Recombination effects in soft-x-ray cluster interactions at the xenon giant resonance

Recombination effects in soft-x-ray cluster interactions at the xenon giant resonance

Edward Ackad[1,3]**, Nicolas Bigaouette**[2]**, Stephanie Mack**[2]**, Konstatin Popov**[2] **and Lora Ramunno**[2]

[1] Department of Physics, Southern Illinois University Edwardsville, Edwardsville, IL 62026, USA
[2] Department of Physics, University of Ottawa, Ottawa, ON K1N 6N5, Canada
E-mail: eackad@siue.edu

Abstract. Xenon clusters in an intense soft-x-ray pulse are examined in detail and compared with recent experimental results by reproducing the experimental signals (Thomas *et al* 2009 *J. Phys. B: At. Mol. Opt. Phys.* **42** 134018). Good agreement is found between our theoretical model and the experimental results. A detailed analysis of the experimental signals and their constituents is performed. We find that, unlike large clusters, the smaller $N = 147$ have a saturated electron kinetic energy distribution (Bostedt *et al* 2010 *New J. Phys.* **12** 083004). We also find the highest charge states which are detected were initially on the outer shell of the cluster whereas the core ions recombine significantly and are detected as only moderately or singly charged (Hoener *et al* 2008 *J. Phys. B: At. Mol. Opt. Phys.* **41** 181001). Further, we find it is the outer shell ions which obtain the highest kinetic energy upon disintegration (Trost *et al* 2012 *Frontiers in Optics Conf.* (Optical Society of America) p FW5G.5).

[3] Author to whom any correspondence should be addressed.

IOP Institute of Physics **ⅅ** DEUTSCHE PHYSIKALISCHE GESELLSCHAFT

Contents

1. Introduction

The x-ray regime has previously been the purview of synchrotrons which are only capable of reaching the linear, single-photon regime. Recent experimental advances now allow for ultra-intense x-ray sources opening a whole new regime of physics [5–7]. This regime is crucial for the development of several areas within nanoscience and its applications, and thus a detailed understanding of this new regime where nonlinear x-ray phenomena may occur is necessary [8–13].

Clusters irradiated with intense, short laser pulses has been a field of continued interest for the past two decades. Many new phenomena have been shown to occur in these systems which bridge the gap between solid and gas phases of matter. Comprehensive reviews on theoretical and experimental methods and results in laser–cluster interactions may be found in [14–16].

Increasingly, laser–cluster interactions are studied in a wavelength regime where single-photon effects are more important than laser-field effects [17–20]. Recently Thomas *et al* [1] explored the interaction in a particularly interesting regime. They examined xenon clusters in the soft-x-ray regime at the giant resonance of atomic xenon. This allowed for a probing of a mechanism fraught with difficulty in measuring: many-body recombination. This built on previous work which showed the importance of recombination in the charge transfer of layered heterogeneous clusters [3]. In all previous (longer wavelength) regimes and with most elements, higher charge states are observed in clusters compared with the gas phase. Xenon has a well known inner-shell resonance [21] centered at around 13 nm, the Auger decay of which leads to multiply charged xenon ions. Thus even in a low intensity beam the singly charged ion signal from a gas is much smaller than the doubly or triply charged signal [22].

In their experiment, Thomas *et al* observed an increase in the singly charged ion signal for clusters, compared with an almost negligible signal in gas. It was clear that some electron–ion recombination was taking place but the details of the experiment, as noted by Thomas *et al*, required further mechanisms beyond photoionization and recombination to completely understand the details of the laser–cluster interaction and subsequent expansion of the cluster [1].

In this work we describe Thomas *et al*'s experiment using our theoretical model. Our microscopic model replicates all the measured signals from the experiment and allows us to

tease out details which are not experimentally accessible. Previous work in this area has focused on explaining the thermal emission of electrons far above the dominant atomic emission line despite the large cluster potential in clusters of $\langle N \rangle = 2000$. It was found to be due to the supra-dense plasma created by the ultra-short, ultra-intense pulse [2].

We find that at the reported intensities, the small clusters are saturated in their thermal emission of electrons at intensities above $2.5 \times 10^{13}\,\mathrm{W\,cm^{-2}}$. We find good agreement with the experimental time-of-flight spectra and our model's results. Our results show that the nanoplasma does not span the entire cluster and the highly charged ions detected come from the outer shell of the cluster. The lower charged states, including the singly charged ion and high velocity atoms, come from the nanoplasma core. They are initially highly charged but recombine with the available plasma electrons and are detected as much lower charged states. The ion kinetic energy was found not to be saturated and the very high energy tail comes entirely from clusters at the peak of the laser pulse. Lastly, we find the expansion of the cluster is best described as a mix of an exploding outer shell and a hydrodynamically expanding core where recombination significantly reduces the charge state of the inner ions.

2. Method

We have significantly extended our previous model [23] in order to incorporate new features relevant for the soft-x-ray regime. The model remains fully microscopic and incorporates photoionization, single-step collisional ionization, collisional excitation and ionization from these excited states in what we term augmented collisional ionization [23]. Further, we have included many-body recombination, Auger decay and multiphoton ionization.

When an inner shell electron is ionized it leaves the atom or ion in an excited state. This state may decay by Auger decay. This occurs when an outer electron decays to the lower, empty, inner state and transfers the energy to other outer electrons which may then ionize or become excited. In the present work, as with Thomas *et al*'s experiment [1], xenon is irradiated with photons of energy matching the center of the giant 4d resonance [21]. The cross-section for photoionization from the inner 4d shell is around ten times larger than from the outer 5p shell [21]. The Auger decay occurs with different decay times depending on the different decay channels. Our model randomly selects a decay channel by taking into account the relative weights of all the possible decay channels. Experimental cross-sections and decay times [22] were used where available and Hartree–Fock calculations were used otherwise [24].

The experimental conditions under consideration also allow for multiphoton ionization, which we implemented similarly to the single-photoionization case [23], but where the laser depletion is by more than one photon. The cross-sections were taken from [25] with some modifications. The four-photon cross-section for the Xe^{13+} and Xe^{14+} was changed to $1 \times 10^{-114}\,\mathrm{cm^8\,s^3}$ to match the Xe^{12+}, and the Xe^{15+} to Xe^{18+} were set to be five-photon processes with a cross-section of $1 \times 10^{-149}\,\mathrm{cm^{10}\,s^4}$. These are underestimates of the multiphoton cross-section in all cases.

Finally, many-body recombination to the ground state was incorporated into our model. Once electrons are ionized from an atom, they are allowed to classically propagate within the cluster. Through collisions, it is possible that an electron may lose enough energy to become classically bound to a single ion. If the energy of an electron is equal to or below the lowest lying empty state of this ion, the electron is considered to have recombined to that ion. It is removed from the code and the ion charge state is decreased by one. To reduce dipole heating,

only electrons less than 1 bohr from an ion are tested for recombination. Recombination not to the ground state but to an excited state is treated classically.

The particles interact at close range as Gaussian charge distributions [23] and at long range using the Coulomb potential. The depth of the potential well of an ion of charge state Z is Z times that of a singly charged ion. Since ionization potentials (Ip) are not strictly linear with Z, the depth of the singly charged ion must be chosen such that all charge states have a potential at $r = 0$ deep enough for recombination to be possible (i.e. potential depth $<$ Ip). Furthermore, the time-step must be small enough not only to prevent accumulating errors during the integration of the equations of motion, but also to prevent electrons from falling too deep into an ion's potential—a situation allowed classically but not quantum mechanically. For the present work a depth of 1 hartree and a time-step of 500 zs are used.

2.1. Propagation to the detector

A full comparison with experimental results ideally requires the propagation of the particles to the detector. This is a challenging endeavor as electrons' motion is on the attosecond time scale while the particles reach the detector on a microsecond time scale. We have thus devised a three-phase strategy to accomplish this with only small approximations.

In the first phase, the cluster interacts with the laser pulse and collisional ionization and recombination both continue for some time afterward. This simulation is run using the shortest time step, and includes all microscopic interactions. Eventually (after about 2 ps for small clusters) ionization becomes infrequent as the cluster disintegrates [26]. Once this happens, phase two is initiated. The ionization routines are switched off in the code, but many-body recombination is still allowed. To increase the efficiency of the calculation, a dynamic time-step is used based on the closest distance between any two particles ($dt \approx R_{\min}/c$ where c is the speed of light). This stage is performed with the time-of-flight field set to the same value as in the experiment of interest. Once the cluster is sufficiently sparse, Rydberg systems are forcibly recombined. This recombination results in a very small underestimate in most cases but makes the long-time propagation feasible by reducing the number of particles. The propagation times for this second phase are around 10 ps.

Once the particles are far enough away from each other, the dominant force they feel is the time-of-flight detector field. The final phase is then initiated. The particles' position and velocity are used as initial conditions to solve Newton's equations of motion for the constant time-of-flight field in a single integration to the field-free region. Then they are propagated in the field-free region to the detector, again with only a single integration step, thereby simulating the whole process of the experiment.

Experimental signals which do not have time-of-flight fields, such as kinetic energy measurements, are performed in the same manner, albeit without the time-of-flight field.

Finally, we incorporate the spatial profile of the laser pulse in our calculations, which is assumed to be Gaussian. We simulate laser–cluster interactions at different intensities, but also consider that clusters at different locations within the laser spatial profile will be at different distances from the detector. Clusters which interact with the wings of the pulse are closer to and farther from the detector than the clusters which interact with the peak of the pulse. This has the effect of broadening the time-of-flight peaks a non-negligible amount as clusters further away will have more kinetic energy (due to more time in the time-of-flight field) while the opposite is true for clusters initially closer to the detector. This was observed virtually as the time-of-flight signals were built up.

3. Recombination in nanoplasmas

Electron–ion recombination is crucial to understanding the results of Thomas *et al*'s experiment. To ensure we have a suitable model for recombination to the ground state, we compare the results of our code to a well-known plasma model for three-body recombination [27]. We compare with a more stringent system than xenon, i.e. argon, as it is three times lighter. The timescale for cluster disintegration is thus shorter for an argon cluster compared with a xenon cluster.

To calculate the recombination rate given by our code, we considered pre-ionized argon clusters of singly charged ions. By enabling our recombination routine (but not the ionization routines), we then can determine numerically the recombination rate as a function of time.

We compare our calculation with a standard three-body recombination model [27]

$$\frac{\mathrm{d}N_\mathrm{i}}{\mathrm{d}t} = \alpha_\mathrm{r} N_\mathrm{e}^2 N_\mathrm{i}, \tag{1}$$

where N_i is the ions density in cm^{-3}, N_e is the electron density in cm^{-3}, $\alpha_\mathrm{r} = 8.75 \times 10^{-27} T_\mathrm{e}^{-4.5}\,\mathrm{cm}^6\,\mathrm{s}^{-1}$ and T_e is the electron temperature in eV. For singly charged ions, $N_\mathrm{i} \approx N_\mathrm{e} \approx N$, then equation (1) becomes

$$\frac{\mathrm{d}N}{\mathrm{d}t} = \alpha_\mathrm{r} N^3. \tag{2}$$

Solving equation (2) yields

$$N(t) = \frac{N_0}{\sqrt{1 + 2N_0^2 \alpha_\mathrm{r} t}}, \tag{3}$$

where $N_0 (\approx 2.8 \times 10^{22}\,\mathrm{cm}^{-3})$ is the initial electron/ion density. Defining the number of recombinations as $N_\mathrm{R}(t) = N_0 - N(t)$ we obtain

$$N_\mathrm{R}(t) = N_0 \left(1 - \frac{1}{\sqrt{1 + t/\tau_\mathrm{r}}} \right), \tag{4}$$

where we defined the recombination time as $\tau_\mathrm{r} = \frac{1}{2\alpha_\mathrm{r} N_0^2}$.

Equation (1) is known to be valid for large systems but we found that it agrees with our simulations of recombination in nanoscopic systems as well. Figure 1 plots N_R as a function of time for our pre-ionized cluster simulations, along with the fits obtained from equation (4). In our simulations, we initialized our pre-ionized clusters with a Maxwell–Boltzmann electron temperature distribution of 13 eV, well within the range expected for laser–cluster nanoplasmas at current experimental conditions. We considered the following argon clusters which are common sizes in cluster experiments: Ar_{5083}, Ar_{1415} and Ar_{147}. We chose clusters of argon (rather than the three-times-heavier xenon) because we wanted to test our recombination model even in the regime where the cluster starts to expand. The points in figure 1 represent our numerically obtained simulation data. The solid lines are a least-squares fit to equation (4), where τ_r a fitting parameter. Since the cluster systems are finite and in motion, $N(t \to \infty) \neq 0$, i.e. not all electrons will recombine. Thus N_0 is also used as a fitting parameter. From the fits, we find that the recombination times for the Ar_{5083}, Ar_{1415} and Ar_{147} clusters are $\tau_\mathrm{r} = 14.0$, 17.8 and 13.4 fs, respectively. These values agree well (within 20%) when compared with the result of equation (4): 15 fs. This good agreement suggests that our recombination model is sufficiently accurate to replicate the dominant features of three-body recombination, even for cluster disintegration.
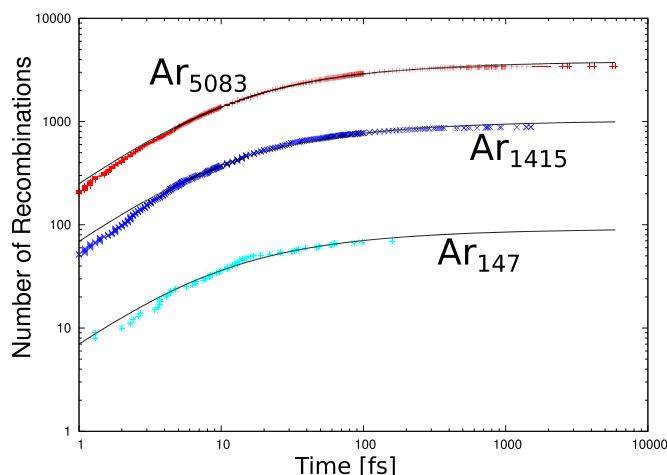
Figure 1. The number of recombinations as a function of time as calculated from singly charged cluster simulations (points). The lines represent fits of these data to the well-known three-body recombination model from [27].

4. Results

A detailed comparison with the experiment described in [1] was performed for xenon clusters with 147 atoms interacting with a $\lambda = 13.7\,\text{nm}$ laser pulse. This was done using the three-phase simulation described in section 2.1, which propagates the particles all the way to the detector. The spatial and time profile of the laser are assumed to be Gaussian. To model the laser–cluster interaction over the laser spatial profile, we simulated 12 intensities ranging from $1 \times 10^{11}\,\text{W cm}^{-2}$ to $5.8 \times 10^{14}\,\text{W cm}^{-2}$ m. Clusters away from the laser focus contribute significantly to the final signal since they are in much larger number than clusters irradiated near the peak intensity. To ensure meaningful statistics, more than three dozen simulations were performed at each intensity. These were integrated to generate results directly comparable to experimental signals.

It is worth noting that a key difference between the experimental signal and the results presented in this work is the influence of uncondensed gas. In most cluster experiments the ion signal from the uncondensed gas is small, if not negligible, especially for high charge states. The current regime differs significantly from this as the laser wavelength is in the middle of xenon's giant resonance. Thus the uncondensed gas produces highly charged ions as is common in x-ray experiments. Nevertheless, good agreement with the experiment is found.

4.1. Electrons

The total kinetic energy spectrum of the electrons is calculated assuming a field-free propagation to the detector. The results are plotted as the blue (upper) line in figure 2 for the complete experimental signal (i.e. all calculated laser intensities are included). An illustration of the pulses intensity is shown in the inset. The kinetic energy distribution decreases close to monotonically until $E \approx 3.5$ hartree. Beyond this a plateau is formed extending to 20 hartree ($\approx 544\,\text{eV}$).

The low energy part of the signal lacks clear atomic peaks as no uncondensed gas was included in the simulation. The spectrum matches qualitatively with the results from [2] despite the difference in cluster size.
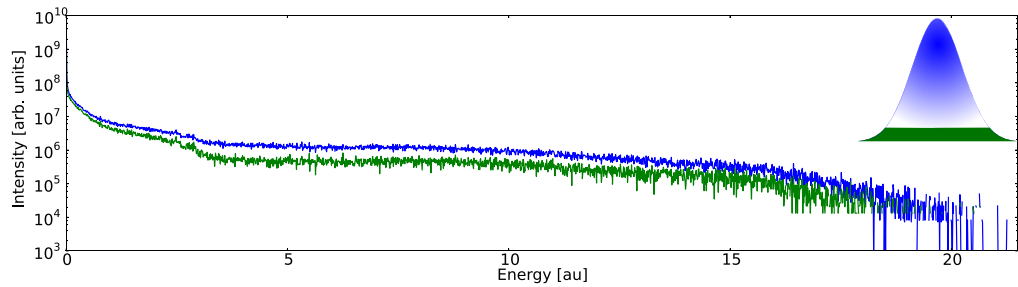
Figure 2. The blue curve is the total electron kinetic energy distribution. The green curve is the normalized total electron kinetic energy distribution without the peak intensities of the laser pulse, $I \geqslant 5 \times 10^{13}\,\mathrm{W\,cm^{-2}}$. Due to the renormalization of the green curve, both have the same number of electrons in the signal. The inset is an illustration of the intensity of the laser pulse for each curve: the blue curve is the entire pulse and the green curve is the pulse when only intensities less than $5 \times 10^{13}\,\mathrm{W\,cm^{-2}}$ are included given the green (lower) shape in the illustration.

To explore the origin of the high energy electron plateau, we replot the curve after removing the contributions of the higher intensities and renormalizing the signal. This is plotted as the green (lower) line in figure 2, which shows the (renormalized) electron kinetic energy distribution excluding contributions from the portions of the laser spatial profile with intensities $\geqslant 5 \times 10^{13}\,\mathrm{W\,cm^{-2}}$. Thus the green (lower) curve shows the electron kinetic distribution from clusters not irradiated by the most intense part of the pulse. Instead it is the clusters irradiated by the green (lower) part of the pulse illustration in the inset. The two distributions are very similar, indicating that the high energy kinetic energy signal is saturated. Removing intensities below $5 \times 10^{13}\,\mathrm{W\,cm^{-2}}$ has a much more dramatic change on the distribution (not shown). The highest energy electrons do not exclusively come from the peak of the laser pulse. Clusters irradiated with the spatial wings of the laser pulse, even at ten times less intensity than the peak, still generate electrons at the highest end of the distribution.

At intensities $\geqslant 5 \times 10^{13}\,\mathrm{W\,cm^{-2}}$ electrons are not accelerated any more than at an intensity of $5 \times 10^{13}\,\mathrm{W\,cm^{-2}}$. The electrons from clusters irradiated at or near the spatial peak of the laser pulse ($\geqslant 5 \times 10^{13}\,\mathrm{W\,cm^{-2}}$) do not have a significantly different distribution of kinetic energy. However, the clusters irradiated at and near the spatial peak of the laser pulse ($\geqslant 5 \times 10^{13}\,\mathrm{W\,cm^{-2}}$) do produce higher charge states (see section 4.2.1) and thus more electrons. Since the clusters at and near the peak generate more electrons, but do not give these electrons more kinetic energy than clusters at outside the spatial peak, we draw the conclusion that the extra electrons quickly leave the cluster and do not increase the electron density of the cluster. Thus the electron kinetic energy distribution signal is saturated and cannot contain a hotter plasma unlike what was seen for larger clusters [2]. This saturation is cluster size dependent, as larger clusters would be able to support a higher electron density. The saturation intensity is thus higher for larger clusters.

4.2. Ions

The properties of the ions from the laser–cluster interaction are now examined. Comparison with experimental signals is shown followed by simplified plots to explain the full composition of the experimental signal.
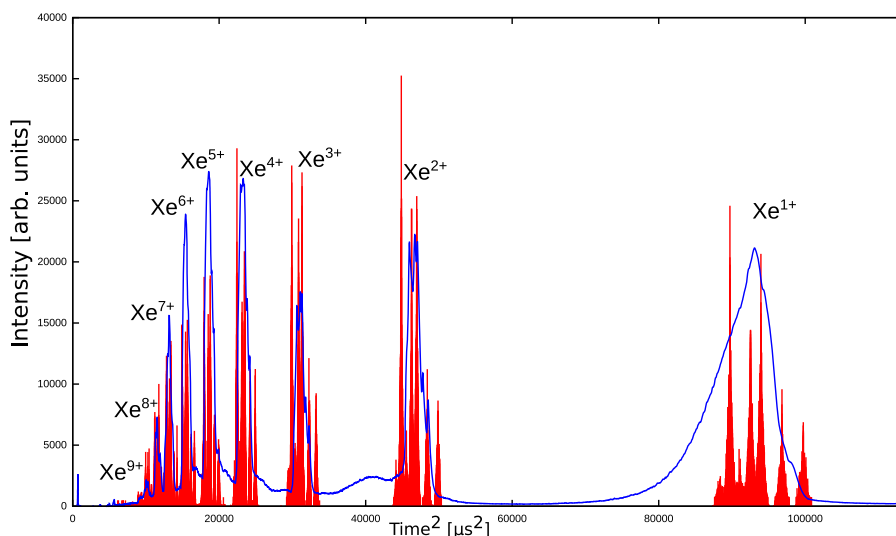
Figure 3. The full time-of-flight ion signal is shown in red including the xenon isotope distribution for xenon clusters of size $N = 147$ irradiated by a 10 fs pulse with $\lambda = 13.7$ eV and $I = 5.8 \times 10^{14}$ W cm^{-2}. The experimental results from [1] are shown as the solid blue line.

4.2.1. Time-of-flight signals. The full time-of-flight signal is shown in figure 3 which includes the mass isotope distribution of xenon. Good agreement is found when compared with the experimental results of [1] shown as the solid (blue) line. In particular, we find a large singly charged ion contribution which was observed experimentally to be dominant only in the cluster signal. As previously mentioned, our simulations do not include uncondensed gas, though it contributes non-negligibly to the experimental signals. This omission is the main contribution to the differences in the relative abundance of each charge state that exist between figure 3 and [1]. Differences in the width of the peaks are primarily caused by the exclusion of the lognormal cluster distribution. The experimental cluster jet contains a distribution of clusters of different sizes and is only peaked at $N = 147$. The other-sized clusters create ions with different kinetic energies. The experimental signal is a convolution of the signal from each size cluster causing much of the broadening [28].

Further analysis of full time-of-flight signal in figure 4(a) is now carried out without including the mass isotope distribution for clarity. Charge states up to Xe^{11+} are now visible as no foot is formed at the high charge states. Further, the width of the peaks may be seen to be decreasing for higher charge states. This will be further explored in section 4.2.3.

To further investigate the origin of the peaks in the time-of-flight signal the full signal is overlaid with partial signals with lower intensities removed. Figure 4(b) shows the full time-of-flight signal in red and the reduced signal from intensities $\geqslant 5 \times 10^{13}$ W cm^{-2} in green. In blue is the reduced signal from intensities $\geqslant 3 \times 10^{14}$ W cm^{-2}. The illustration in the singly charged box shows the portion of the pulse used to construct each of the distributions. The distributions in each box use different scales (both vertical and horizontal).

The high charge states (Xe^{7+} and above) emerge primarily from the very highest intensity spatial regions of the pulse. The Xe^{7+} charged states and above are almost exclusively created in intensities higher than $I \geqslant 5 \times 10^{13}$ W cm^{-2} (shown in green). The very highest intensities,
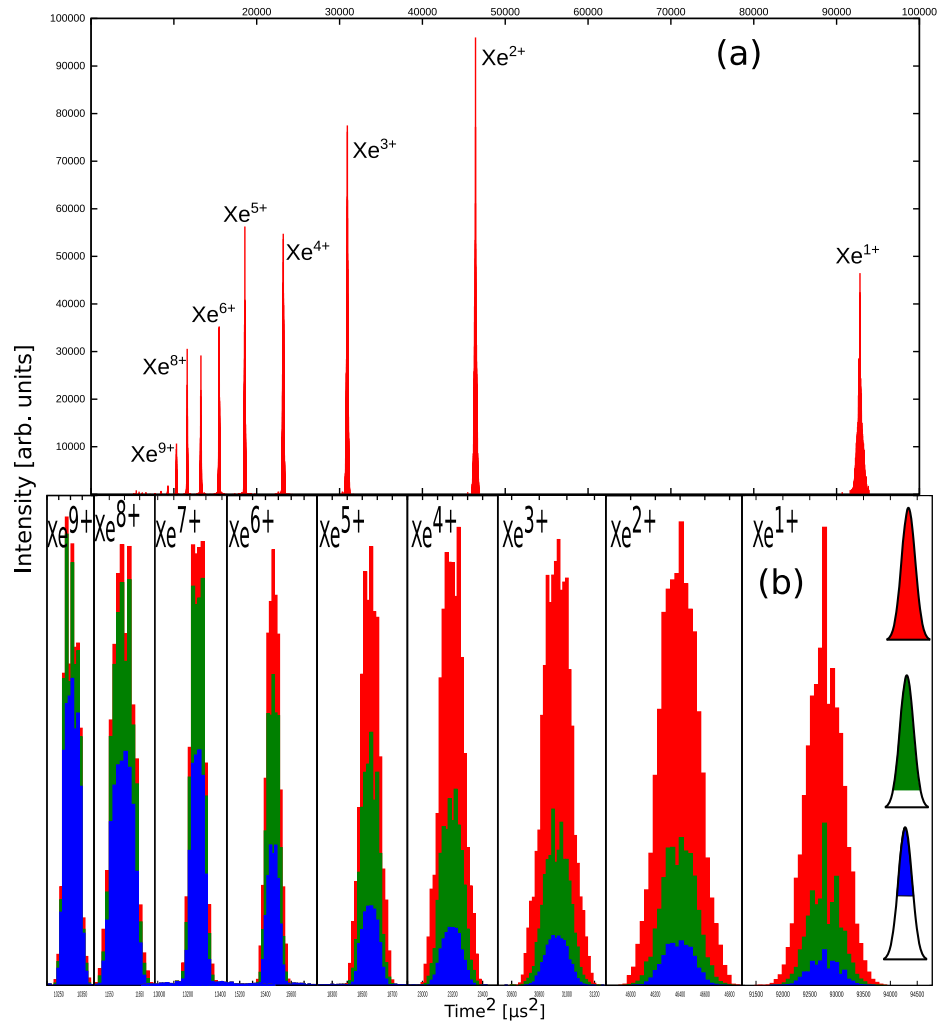
Figure 4. (a) The time-of-flight signal without mass isotopes. (b) Comparison of the full (single-isotope) time-of-flight signal in red with the time-of-flight signal from $I \geqslant 5 \times 10^{13}\,\mathrm{W\,cm^{-2}}$ only shown in green and $I \geqslant 3 \times 10^{14}\,\mathrm{W\,cm^{-2}}$ only shown in blue. Each charge state is on a different scale. The illustration on the right of the singly charged distribution shows the part of the pulse used to construct each distribution on a linear scale.

$I \geqslant 3 \times 10^{14}\,\mathrm{W\,cm^{-2}}$ (shown in blue) irradiate a smaller number of clusters but still generate more than 30% of the Xe^{7+} charged states and above. The higher charged states, Xe^{10+} and above, are almost exclusively created by the highest intensities, $I \geqslant 3 \times 10^{14}\,\mathrm{W\,cm^{-2}}$ (not shown).

The Xe^{1+} signal on the other hand emerges from the lower intensity regions. This remains true even when considering the relative number of clusters in the spatial region: the lower intensities will irradiate more clusters compared with the higher intensities and thus any signal from the lower intensities is amplified. Including this, the relative number of Xe^{1+} compared with the total number of atoms in the spatial region of the pulse, i.e. the fraction of Xe^{1+} per atom, the Xe^{1+} is still far more abundant in the low intensity region.
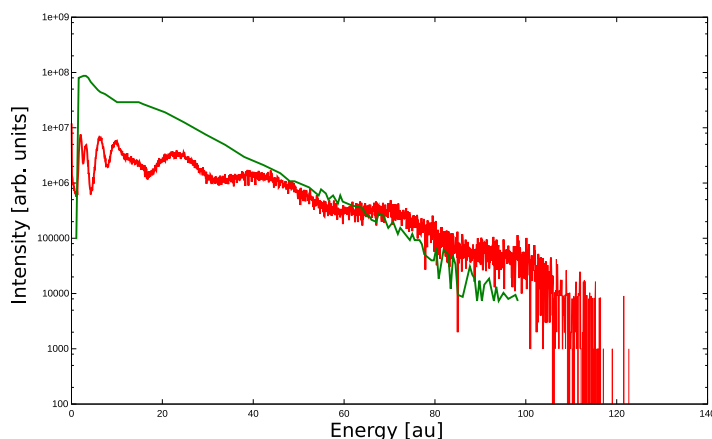
Figure 5. The IKED from [1] is shown as the solid (green) line and the results of this work are shown as the thick (red) line.

The widths of each reduced intensity peak in figure 4(b) give information about the contribution of different intensities to the high energy ions of a charge state. The highest energy ions of a charge state come from the highest intensity regions of the pulse. This is discernible from the asymmetry toward smaller times for the time-of-flight signals of the high intensity signal (blue and to a lesser extent green). However, for low charge states, the contribution from the very highest intensity is small. This is due to the proportionally smaller number of lower charge states and the smaller number of irradiated clusters, i.e. the high intensity part of the pulse irradiates few clusters and the intensity is so high that few Xe^{1+} are produced. Xe^{1+} are rarely produced by direct photoionization and are predominantly produced by three-body recombination.

4.2.2. Total kinetic energy distributions. The ion kinetic energy distribution (IKED) for $\langle N \rangle = 150$ was reported in [1] using a combination of the time-of-flight data and simulations. In figure 5 their results are shown as the (green) line to compare with our total IKED results shown as the thick (red) line. We find good agreement at the high energy region. Our results show a cut-off just above what the experimental detector found near 100 hartree (≈ 2.7 keV).

There is, however, disagreement at lower energies. We find that this disagreement stems from a combination of uncondensed gas and clusters of different sizes which occur in the cluster's beam [28]. The smaller clusters ($N < 147$) and uncondensed gas create ions with significantly less kinetic energy and are included in the experimental signal but absent in this work. In [1], Thomas *et al* find that smaller clusters have a more rapidly decreasing high energy tail compared with larger clusters. Thus the experimental signal for $\langle N \rangle = 150$ will have a significant contribution from $\langle N \rangle = 55$ and produce a discrepancy at the low energy regime.

The solid (green) curve in figure 6(a) shows the reduced IKED signal when only intensities up to 2.5×10^{13} W cm^{-2} are included compared with the full signal in blue. This is illustrated in the spatial intensity profile in the inset for each curve. The low energy part of the IKED remains almost unchanged, except for the peak near 3.3 hartree which is absent. A sharp cut-off is seen in the reduced signal around 10 hartree (≈ 270 eV). While the peak near 25 hartree is somewhat reproduced the very high energy ions are absent from the reduced signal.

The solid (green) curve in figure 6(b) shows the reduced signal when only intensities up to 5×10^{13} W cm^{-2} are included as illustrated in the inset by the green (lower) cut-off pulse shape.
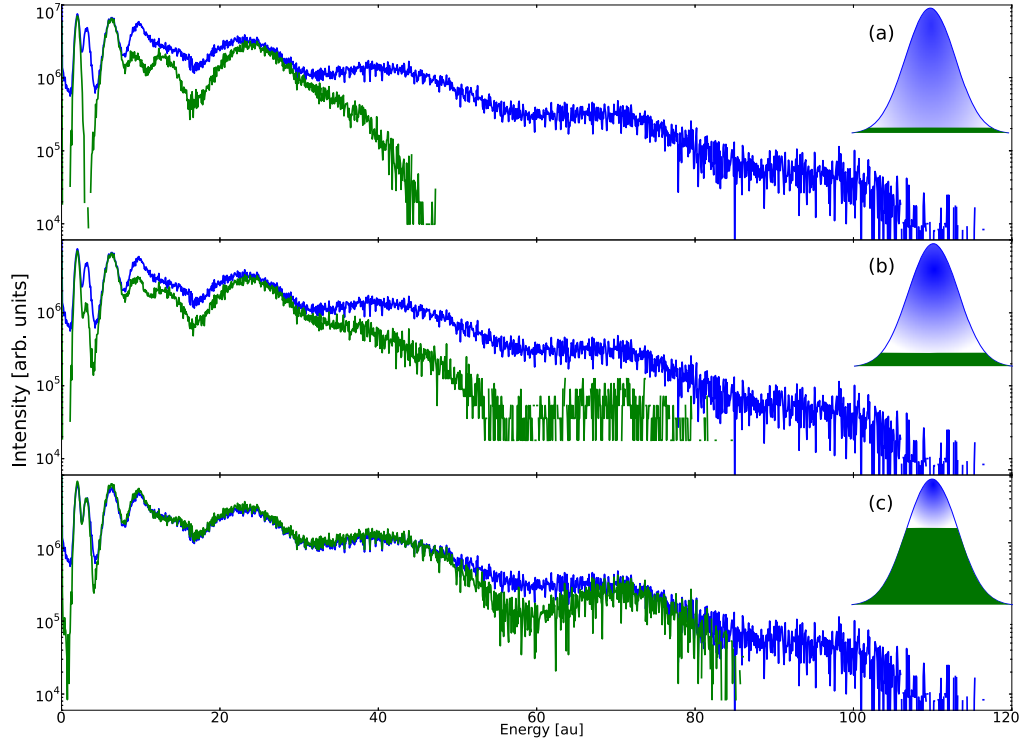
Figure 6. (a) The total ion kinetic energy in blue and the total ion kinetic energy excluding $I \geqslant 2.5 \times 10^{13}\,\mathrm{W\,cm}^{-2}$ in green. (b) The total ion kinetic energy in blue and the total ion kinetic energy excluding $I \geqslant 5 \times 10^{13}\,\mathrm{W\,cm}^{-2}$ in green. (c) The total ion kinetic energy in blue and the total ion kinetic energy excluding $I \geqslant 3 \times 10^{14}\,\mathrm{W\,cm}^{-2}$ in green. The insets are an illustration of the spatial intensity of the laser pulse for each curve: the blue curve is the entire intensity profile of the pulse and the green part is an illustration of the included intensities in the green curve.

Two new peaks now appear at 3.3 and 70 hartree. These peaks are thus largely the result of clusters irradiated at $\approx 2.5 \times 10^{13}\,\mathrm{W\,cm}^{-2}$.

The solid (green) curve in figure 6(c) shows the reduced signal when only intensities up to $3 \times 10^{14}\,\mathrm{W\,cm}^{-2}$ are included. The low energy region matches well with the full signal demonstrating that the clusters irradiated near the spatial peak of the laser pulse do not produce a significant amount of ions below 25 hartree. The high energy tail, however, is almost exclusively created by clusters near the spatial peak. Thus the high energy IKED is not saturated, unlike the high energy electron kinetic energy distribution, as discussed in section 4.1.

Different spatial regions of the pulse thus contribute differently to the IKED. As expected, the highest kinetic energy ions are produced by clusters irradiated by the spatial peak of the laser pulse. This is seen by examining the difference between the green and blue curves in figure 6(a) and noticing that the green curve ends near 85 hartree. Ions with kinetic energy above 85 hartree can only be produced when the cluster is irradiated with more than $3 \times 10^{14}\,\mathrm{W\,cm}^{-2}$. The low kinetic energy region is largely produced by clusters in the spatial wings of the pulse which are not irradiated with the peak intensity. The peak at 3.3 hartree, which is produced by the high intensity part of the pulse, is due to the disintegration of an inner shell of the cluster.
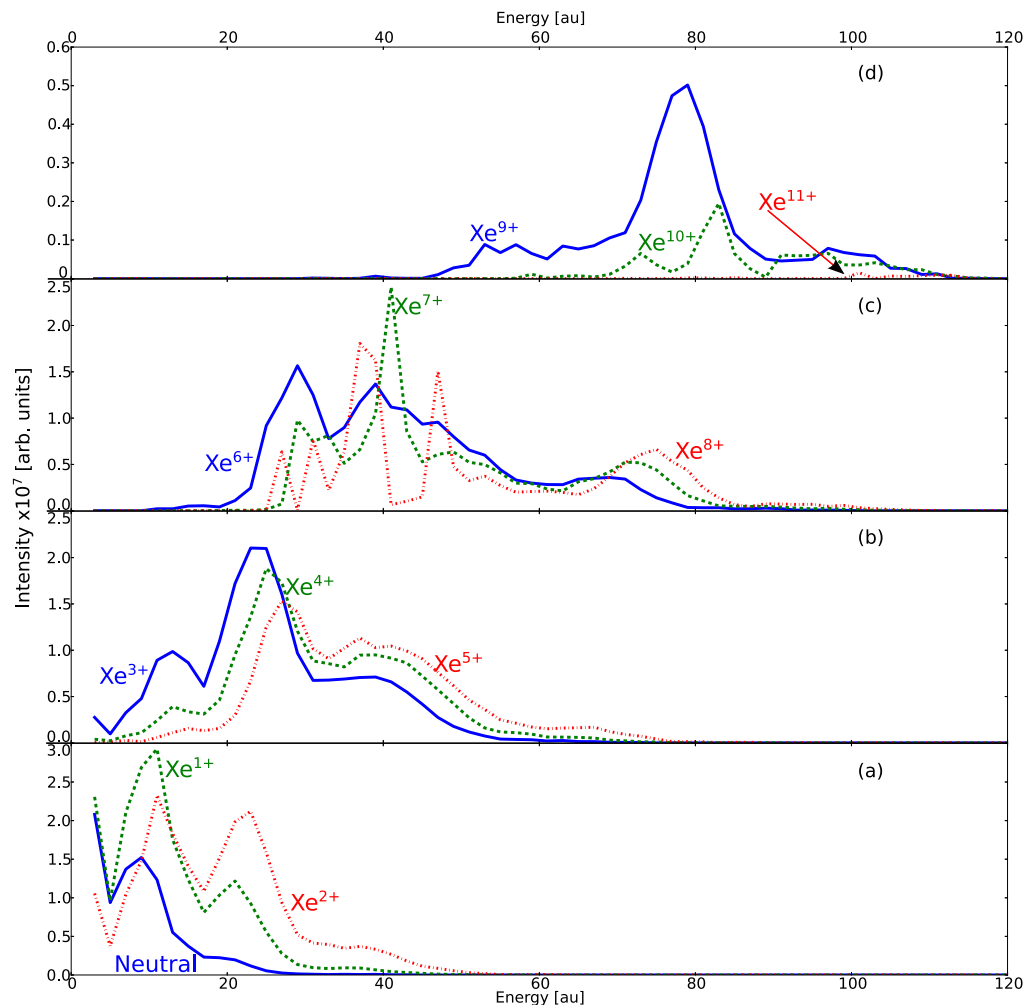
Figure 7. The kinetic energy distribution of the ionic states (a) 0–2, (b) 3–5, (c) 6–8 and (d) 9–11.

At the higher intensities there are more electrons which have escaped the cluster (see figure 2 and the explanation therein) leaving a larger charged core during the disintegration. The inner shell, more highly charged near the spatial peak of the pulse, gains more kinetic energy upon disintegration, forming the peak at 3.3 hartree.

4.2.3. Individual kinetic energy distributions. To further understand the expansion dynamics of the cluster, the IKED is now separated for each charge state. Figure 7(a) gives the IKED for the neutral (although undetectable in current experimental setups) as a solid (blue) line, the Xe^{1+} as a dashed (green) line and the Xe^{2+} as a dotted (red) line. Figures 7(b)–(d) give the IKED for the Xe^{3+} to Xe^{11+}, with the same respective curve styles as (a).

The plots in figure 7 are not normalized and thus show the relative abundance of each charge state as well. The IKED and abundance for the three charge states in figure 7(a) have peaks at the same energies except for the peak near 22 hartree which is largely suppressed in the neutrals. These curves resemble the Xe^{3+} curve in figure 7(b) for energies below around 35 hartree. Recombination thus significantly reduces the charge state of the low energy ions to predominantly less than Xe^{4+}.
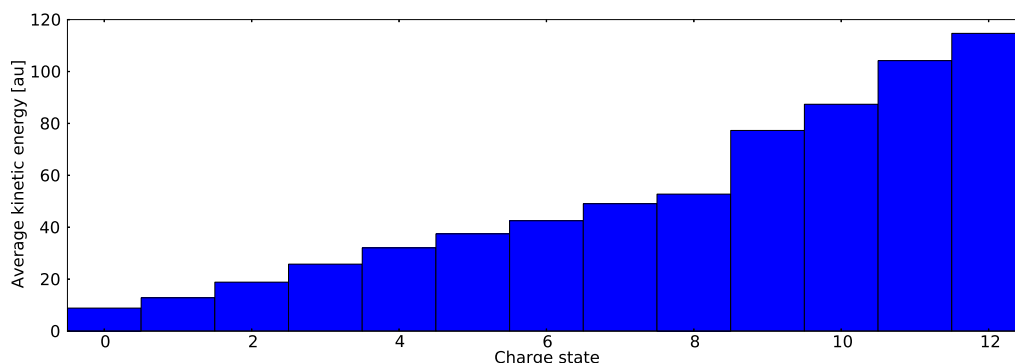
Figure 8. The average ion kinetic energy for each charge state.

The persistence of the peaks in figures 7(a) and (b) across multiple charge states suggest they are of a common origin. Higher charge states in the core of the cluster gain their kinetic energy during the initial disintegration of the core. During the disintegration some recombination occurs. This causes newly recombined ions to still have the same kinetic energy as their higher-charged brethren, thus giving the same peak across multiple charged states. This indicates that those ions were largely outside the cluster potential before the recombination occurred. The recombination thus mostly takes place after the disintegration of the cluster's core.

This must occur through recombination as high energy neutrals are also produced, with the same IKED peak locations as Xe^{1+} to Xe^{4+}. In fact there is a sizable peak around 9 hartree which corresponds to neutrals with a temperature of 2.8 million K. This peak is weakly present in the Xe^{5+} signal but increases significantly as the charge state is lowered peaking with Xe^{2+} but remaining large even for neutrals.

The differences between the low charge states ($<Xe^{4+}$) are predominantly at the high energy tail of the IKED due to the reduced probability of three-body recombination for fast moving ions. The lower charge states emerge from a common pool of ions and then recombine to lower charge states and thus produce IKED peaks in similar locations. The higher charged ions have IKED peaks at different energies showing that they are not part of the common pool of ions that will recombine to form the lower charge state ions. The higher charge states are in fact mainly from the outer shells of the clusters. The lower charge states are from the core of the cluster. The nanoplasma which formed in the core thus produces high charge states initially but upon disintegration most of these ions recombine to charge states below Xe^{5+}.

By integrating the curves in figure 7 for each charge state, we calculate the average ion kinetic energy for each charge state, shown in figure 8. A clear increase in the average kinetic energy of each charge state is found. The increase is gradual and does not have a unit linear slope in the charge state, i.e. the value for Xe^{4+} is not twice that of Xe^{2+}. The relationship between charge state and ejection energy is higher and closer to a linear relationship for charge states $Xe^{1}+$ to $Xe^{8}+$ compared with the quadratic relationship found in [1].

However, this is expected as only clusters of size $N = 147$ were included in our work. Smaller clusters, which are present in the experimental cluster beam, would significantly lower the average ejection energy.

The higher charge states, $>Xe^{9+}$, are infrequent, occurring more than four times fewer than even the Xe^{8+}. Because of this, we would need to do a larger number of simulations to determine
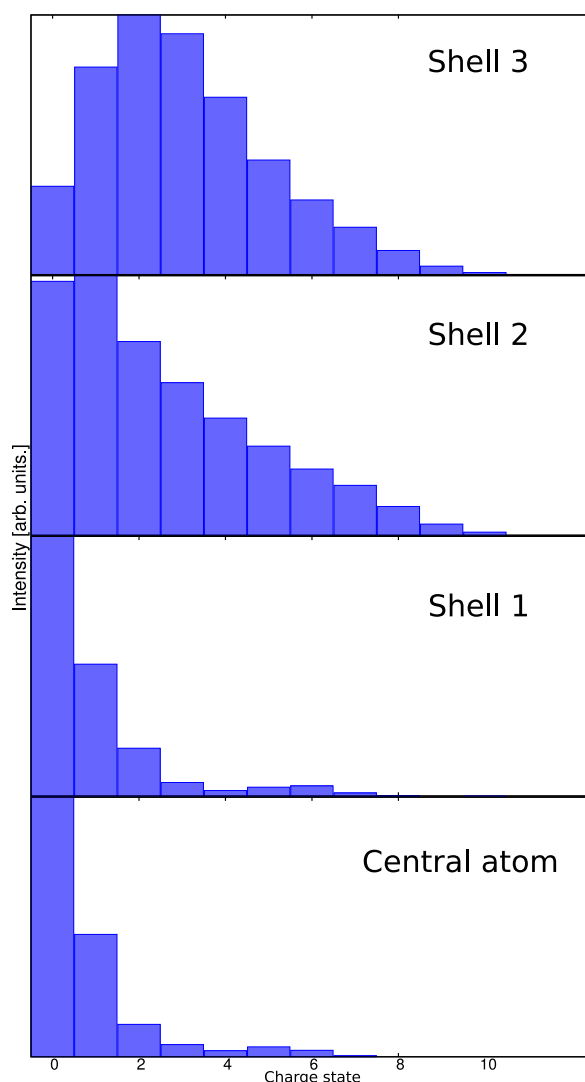
Figure 9. The charge state distributions for the central atom and the three shells of the 147 Xe clusters.

their properties more accurately. Nevertheless, our observation that they carry a considerable amount of kinetic energy upon disintegration is qualitatively correct, and borne out in both figures 7(d) and 8.

In conclusion, the highest charge states are thus found to be produced in the most intense spatial region of the laser pulse profile (cf figure 4(b)) and are the ions with the highest kinetic energy.

4.2.4. Relationship between the initial position of an atom and its final charge state. Having tracked the final detector states and obtained their kinetic energy, it is also possible to examine the relationship between the initial position of the atoms within the cluster, and their final charge state. Atomic clusters are roughly icosahedral shelled structures, and thus the position of an atom relative to its cluster center can be characterized by the shell from which it originated. There are three shells in a 147-atom cluster, plus a single central atom. The final charge state distributions

resulting from each shell (and the central atom), are plotted in figure 9 for the entire laser profile (all intensities integrated with their relative abundance).

We find that the highest charge states all originate from atoms in the outermost shell of the cluster (shell 3) [4]. While the physical center of the cluster produces higher charge states during the laser–cluster interaction [26], in the soft-x-ray regime, these recombine to much lower charge states (including neutral) prior to detection. Most of the neutrals from the outer shell are atoms that are simply never ionized due to being in the low intensity region of the laser's spatial profile.

The primary contribution to the Xe^{1+} signal comes from the inner shells of the cluster, and even more so from shell 1 than shell 2. This is due to the center of the cluster's nanoplasma being quasi-neutral and dense, allowing for efficient three-body recombination. Further from the center of the cluster the density decreases and thus the recombination rate also decreases. This makes the recombination to lower charge states less probable in the outer shell.

5. Conclusion

A detailed investigation into the results of Thomas *et al*'s xenon clusters in an ultra-intense resonant laser pulse has been performed. The time-of-flight signal was reproduced and analyzed to determine the role of the high and low intensity components of the laser pulse. The kinetic energy distribution of the electrons was found to be saturated at an intensity of 5×10^{13} W cm^{-2} while the ion's kinetic energy distribution was not. A detailed examination of the kinetic energy distribution of each charge state revealed that high energy neutrals are produced and that the lower charge states must come from a common pool of ions. Further, the highest charge states detected come from the outer shell of the cluster and these carry away the most amount of kinetic energy. Lower charge states were created via recombination and originated primarily from inner shells.

Acknowledgments

References

[1] Thomas H, Bostedt C, Hoener M, Eremina E, Wabnitz H, Laarmann T, Plönjes E, Treusch R, de Castro A R B and Möller T 2009 Shell explosion and core expansion of xenon clusters irradiated with intense femtosecond soft x-ray pulses *J. Phys. B: At. Mol. Opt. Phys.* **42** 134018
[2] Bostedt C, Thomas H, Hoener M, Möller T, Saalmann U, Georgescu I, Gnodtke C and Rost J-M 2010 Fast electrons from multi-electron dynamics in xenon clusters induced by inner-shell ionization *New J. Phys.* **12** 083004
[3] Hoener M, Bostedt C, Thomas H, Landt L, Eremina E, Wabnitz H, Laarmann T, Treusch R, a De Castro R B and Möller T 2008 Charge recombination in soft x-ray laser produced nanoplasmas *J. Phys. B: At. Mol. Opt. Phys.* **41** 181001
[4] Trost J, Ackad E, Bigaouette N and Ramunno L 2012 Explosion of non-spherical clusters due to irradiation with intense femtosecond x-rays *Frontiers in Optics Conf.* (Optical Society of America) p FW5G.5

[5] Gorkhover T *et al* 2012 Nanoplasma dynamics of single large xenon clusters irradiated with superintense x-ray pulses from the linac coherent light source free-electron laser *Phys. Rev. Lett.* **108** 245005

[6] Thomas H 2012 Explosions of xenon clusters in ultraintense femtosecond x-ray pulses from the LCLS free electron laser *Phys. Rev. Lett.* **108** 133401

[7] Foucar L *et al* 2012 Ultra- atoms by intense x-ray free-electron laser pulses *Nature Photon.* **6** 858–65

[8] Doumy G *et al* 2011 Nonlinear atomic response to intense ultrashort x rays *Phys. Rev. Lett.* **106** 083002

[9] Richter M, Amusia M Ya, Bobashev S V, Feigl T, Juranić P N, Martins M, Sorokin A A and Tiedtke K 2009 Extreme ultraviolet laser excites atomic giant resonance *Phys. Rev. Lett.* **102** 163002

[10] Lambropoulos P, Nikolopoulos G M and Papamihail K G 2011 Route to direct multiphoton multiple ionization *Phys. Rev.* A **83** 021407

[11] Schorb S *et al* 2012 Size-dependent ultrafast ionization dynamics of nanoscale samples in intense femtosecond x-ray free-electron-laser pulses *Phys. Rev. Lett.* **108** 233401

[12] Rudek B *et al* 2013 Resonance-enhanced multiple ionization of krypton at an x-ray free-electron laser *Phys. Rev.* A **87** 023413

[13] Bostedt C *et al* 2012 Ultrafast x-ray scattering of xenon nanoparticles: imaging transient states of matter *Phys. Rev. Lett.* **108** 093401

[14] Saalmann U, Siedschlag Ch and Rost J M 2006 Mechanisms of cluster ionization in strong laser pulses *J. Phys. B: At. Mol. Opt. Phys.* **39** R39

[15] Bostedt C, Adolph M, Eremina E, Hoener M, Rupp D, Schorb S, Thomas H, de Castro A R B and Müller T 2010 Clusters in intense flash pulses: ultrafast ionization dynamics and electron emission studied with spectroscopic and scattering techniques *J. Phys. B: At. Mol. Opt. Phys.* **43** 194011

[16] Th. Fennel, Meiwes-Broer K-H, Tiggesbäumker J, Dinh P M and Suraud E 2010 Laser-driven nonlinear cluster dynamics *Rev. Mod. Phys.* **82** 1793–842

[17] Fennel T, Ramunno L and Brabec T 2007 Highly charged ions from laser–cluster interactions: local-field-enhanced impact ionization and frustrated electron–ion recombination *Phys. Rev. Lett.* **99** 233401

[18] Siedschlag C and Rost J-M 2004 Small rare-gas clusters in soft x-ray pulses *Phys. Rev. Lett.* **93** 043402

[19] Santra R and Greene C H 2003 Xenon clusters in intense VUV laser fields *Phys. Rev. Lett.* **91** 233401

[20] Ziaja B *et al* 2009 Energetics, ionization and expansion dynamics of atomic clusters irradiated with short intense vacuum-ultraviolet pulses *Phys. Rev. Lett.* **102** 205002

[21] Becker U, Prescher T, Schmidt E, Sonntag B and Wetzel H E 1986 Decay channels of the discrete and continuum xe 4d resonances *Phys. Rev.* A **33** 3891–9

[22] Uiberacker M *et al* 2007 Attosecond real-time observation of electron tunnelling in atoms *Nature* **446** 627–32

[23] Bigaouette N, Ackad E and Ramunno L 2011 Augmented collisional ionization via excited states in XUV cluster interaction *J. Phys. B: At. Mol. Opt. Phys.* **44** 165102

[24] Cowan R D 1981 *The Theory of Atomic Structure and Spectra* (Berkeley, CA: University of California Press)

[25] Makris M G, Lambropoulos P and Mihelič A 2009 Theory of multiphoton multielectron ionization of xenon under strong 93 eV radiation *Phys. Rev. Lett.* **102** 033002

[26] Ackad E, Bigaouette N, Briggs K and Ramunno L 2011 Clusters in intense XUV pulses: effects of cluster size on expansion dynamics and ionization *Phys. Rev.* A **83** 063201

[27] *Plasma NRL Formulary* 2009 Naval Research Laboratory, pp 54–5

[28] Arbeiter M and Fennel T 2010 Ionization heating in rare-gas clusters under intense XUV laser pulses *Phys. Rev.* A **82** 013201